A highly porous metal-organic framework system to deliver payloads for gene knockdown

Michelle H. Teplensky[a], Marcus Fantham[b], Chetan Poudel[b], Colin Hockings[c], Meng Lu[c], Alina Guna[d], Marta Aragones-Anglada[a], Peyman Z. Moghadam[a,e], Peng Li[f], Omar K. Farha[f,g], Sandra Bernaldo de Quirós Fernández[h], Frances M. Richards[h], Duncan I. Jodrell[h], Gabriele Kaminski Schierle[c], Clemens F. Kaminski[b,*], and David Fairen-Jimenez[a,*,φ]

[a]Adsorption & Advanced Materials Laboratory (AAML), Department of Chemical Engineering & Biotechnology, University of Cambridge, Philippa Fawcett Drive, Cambridge CB3 0AS, UK

[b]Laser Analytics Group, Department of Chemical Engineering & Biotechnology, University of Cambridge, Philippa Fawcett Drive, Cambridge CB3 0AS, UK

[c]Molecular Neuroscience Group, Department of Chemical Engineering & Biotechnology, University of Cambridge, Philippa Fawcett Drive, Cambridge CB3 0AS, UK

[d]MRC Laboratory of Molecular Biology, Cambridge CB2 0QH, UK

[e]Department of Chemical and Biological Engineering, University of Sheffield, Mappin Street, Sheffield S1 3JD, UK

[f]Department of Chemistry, Northwestern University, Evanston, Illinois 60208, USA.

[g]Department of Chemical and Biological Engineering, Northwestern University, Evanston, IL, 30208, USA.

[h]Cancer Research UK Cambridge Institute, University of Cambridge, Cambridge CB2 0RE, UK.

*e-mail: cfk23@cam.ac.uk, df334@cam.ac.uk. φLead author

Since it was first reported a few decades ago, RNA interference (RNAi) has become a widely used research tool for cellular genetic knockdown. However, its instability and susceptibility to enzymatic degradation has prevented its widespread adoption for use in clinic, and thus major research efforts are directed at seeking methods to protect the fragile RNA payload during delivery. Here, we report the use of a metal-organic framework (MOF) to load, protect, and deliver small interfering ribonucleic acids (siRNA). We confirmed protection of MOF-internalized siRNA from enzymatic degradation. Furthermore, through combined encapsulation of siRNA in the MOF with a variety of additional cofactors (proton sponge, KALA peptide and NH4Cl) we show that endosomal retention can be evaded and we ensure the efficacy of gene knockdown. *In vitro* studies after siRNA/MOF complexation demonstrated consistent levels of knockdown of up to 27%. We use structured illumination super-resolution microscopy (SIM) to study the endocytic uptake of the complex. Overall, we demonstrate the potential of these highly porous and biodegradable materials as a means to improve both efficacy and efficiency of future gene therapies.

Every year, more than 14 million people are diagnosed with cancer, and more than 1 in 3 people will develop some form of cancer during their lifetime.[1,2] Although there are great advances in terms of diagnosis and treatment, cancer remains a key societal health concern. Depending on cancer type and stage, common treatments include surgical resection, chemo- and radiotherapy.[3] The key to success of these treatments lies in early detection, screening, and improvements in the treatment technologies.[4] In many cases, however, complete tumor resection is not feasible due to the invasive nature of required procedures, making local recurrence inevitable. In addition, many patients are not suitable for surgery due to co-morbidities or proximity of tumors to vital structures. This is particularly critical for hard-to-treat cancers such as ovarian, malignant mesothelioma, triple-negative breast, and pancreatic cancer – where five-year survival rates have not improved in the last 20 years and are still around 10%.[5,6] For these cancers, common treatments are not successful and there is an imperative need to develop novel therapeutic approaches.

One such approach is the use of small interfering ribonucleic acids (siRNAs) for gene knockdown expression of key cancer driver genes, which has received great attention over recent years.[7–9] This method is attractive because it i) has a high efficiency of knockdown, ii) is highly specific and thus exhibits minimal off-target effects, and iii) has a lack of systemic toxicity and immunoreactivity.[10] Various medical diseases in addition to cancer, including neurological disorders and viral infections, may in the future benefit from siRNA gene therapies.[11,12] siRNA is a double-stranded RNA fragment typically twenty-one to twenty-three nucleotides in length that can code for a particular cellular gene, cleaved from endogenously expressed long double-stranded RNAs (dsRNAs).[13] Synthetically-created siRNAs have potential as inhibitors of various disease-associated genes, bypassing the first step of endogenous cleavage, and allowing for the creation of a platform technology with any genetic sequence. The mechanism for siRNA delivery and subsequent gene knockdown is universal for any selected sequence,

58 giving it targeted therapeutic potential.[11] This is in contrast to drugs currently used in cancer therapies –

59 including doxorubicin, 5-fluorouracil or docetaxel – which may act on multiple pathways.[14]

60   Although siRNA therapy has potential to benefit patients with cancer, the main limitation is its lack

61 of stability and ease of degradation by native biological enzymes.[15,16] In addition, while non-encapsulated

62 small molecule drugs can enter the cell cytoplasm directly through the plasma membrane, macromolecule

63 delivery into cytoplasm is challenging. To overcome this problem, researchers have altered the chemical

64 structure of siRNAs through modifications to the phosphodiester, sugar backbone, or have changed bases

65 in the sequence.[17,18] There has been some success with chemical modifications to siRNAs,[19,20] such as

66 improving duplex stability and conferring nuclease resistance by replacing the 2'-hydroxyl of the ribose;

67 modification of a few residues has been generally well tolerated.[21] However, chemical modifications are

68 sequence dependent and can require tailoring for different siRNAs. Additionally, chemical modification

69 tends to lower the therapeutic efficacy of the siRNAs upon cytosolic delivery. An alternative approach

70 is the incorporation, and thus protection, of siRNAs as a payload within polymers or nanoparticles.[22–24]

71 Some examples are organic delivery vehicles, such as liposomes or nanoparticles, to carry siRNAs into

72 the cell, protecting it from degradation in the extra-cellular space. However, liposomes tend to

73 accumulate in the reticuloendothelial system[16] and some formulations of nanoparticles can only achieve

74 low loading capacities due to the low negative charge and intrinsic stiffness of double-stranded

75 siRNA.[22,25,26]

76   In this context, metal−organic frameworks (MOFs), a class of porous self-assembled materials

77 composed of metal ions/clusters connected by organic linkers, are one of the most promising materials

78 for biomedicine.[27–31] There are currently more than 84,000 MOF structures in the Cambridge Structural

79 Database and the diversity that MOFs offer is of particular interest for siRNA delivery. Others have

80 utilized MOFs for the delivery of siRNAs and other biomacromolecules, such as CRISPR/Cas9

81 machinery.[29,32,33] However, in these cases, the selected biocompatible MOFs do not contain pore

3

82   dimensions large enough to allow for internally adsorbed siRNAs.[29,33] Additionally, in the case with

83   CRISPR/Cas9, the synthesis had to be altered to build the framework (ZIF-8) around the

84   biomacromolecule machinery,[32] limiting in principle the scope of frameworks feasible with this method,

85   as well as incorporating a zinc-based moiety that has been shown in literature to be toxic even at low

86   concentrations.[34] By selecting appropriate MOFs that can provide large pore sizes, we allow for the

87   encapsulation of macromolecules and their subsequent protection, increasing their bioavailability within

88   the tumor whilst avoiding off-target toxicity.[27] Among the different MOFs, we and others have utilized

89   zirconium-based MOFs (Zr-MOFs) for a variety of reasons.[35,36] They have been shown to be stable in

90   water, a useful characteristic for loading the MOFs with a biological payload, and demonstrate a lack of

91   toxicity and high thermal, mechanical, and chemical stabilities. Importantly, however, these MOFs have

92   no long-term stability in biological solvents where their breakdown prevents potentially in vivo

93   accumulation.[31] In this work, we bring together a combination of multidisciplinary tools to develop a

94   MOF-based platform for the encapsulation of siRNAs and its successful delivery into cells. We explore

95   the mechanism through which the MOF is able to protect the siRNA from degradation in the extra-

96   cellular space, and also how the siRNA is released from the MOF and delivered to the cytosol to become

97   active in the cell. We also prove that the system leads to the specific knockdown of a targeted gene.

98   Design of cell system and corresponding siRNAs

99   We utilized a previously designed HEK 293 cell line[40] (referred here as HEK 293-mC) based on the

100   commercially available T-REx Flp-In system, where mCherry fluorescence expression can be induced

101   using doxycycline or tetracycline (dox or tet). To coordinate an siRNA sequence with the mCherry gene

102   genetically engineered into the HEK 293-mC cells, we designed a custom siRNA sequence. We sought

103   a sequence that limited off-target effects and effectively coded for the inducibly expressed mCherry

104   protein. From the genetic code of the mCherry used, 5 out of 32 21-nucleotide length sequences were

105   identified as promising candidates due to their low GC content (<50%) and no stretches of greater than

106   4 T or A basepairs, as literature demonstrated these considerations improve activity.[41,42] We evaluated

107   these 5 siRNAs loaded on lipofectamine qualitatively using microscopy and western blot analysis to

108   determine whether there was any knockdown in intracellular mCherry signal; **Table S1**, in the

109   Supplementary Information, lists the 5 identified siRNAs. **Figure 1a** shows optical microscopy images

110   of 4 siRNA control conditions after they are incubated with HEK 293-mC cells, some of which are

111   doxycycline-induced; **Figure S1** shows the quantitative intensity analysis of the microscope images.

112   When not induced (i.e. -dox in **Fig. 1a**), the cells show no visible fluorescence, whereas when induced

113   (i.e. +dox) and not siRNA treated ("no treatment"), the cells fluoresce. To demonstrate that only a specific

114   targeted siRNA sequence leads to knockdown of the mCherry fluorescence, we used a "scrambled

115   siRNA." Differences in brightness levels between cells treated with scrambled siRNAs and those with

116   no treatment were not significant, verifying that the random sequence has no effect on mCherry

117   knockdown. When reverse transfecting the 5 different custom siRNAs with the cells in **Figure 1b**, the

118   brightness of the red signal varies between different siRNA strands. This indicates that siRNA 2, 3, 17,

119   28, and 29 had differential knockdown efficiencies for mCherry, with siRNA 3 and 28 appearing to be

120   most effective. This is clear in the western blot (**Fig. 1c**), where bands for anti-RFP antibody for samples

121   3 and 28 are noticeably less intense than any other band of mCherry induced cells. A Ponceau stain shows

122   equal loading of all samples (**Fig. 1d**). For all subsequent experiments, we utilized siRNA sample 3 as a

123   double-stranded sequence with the sense strand 5' – AAGGAGTTCATGCGCTTCAAG – 3'.
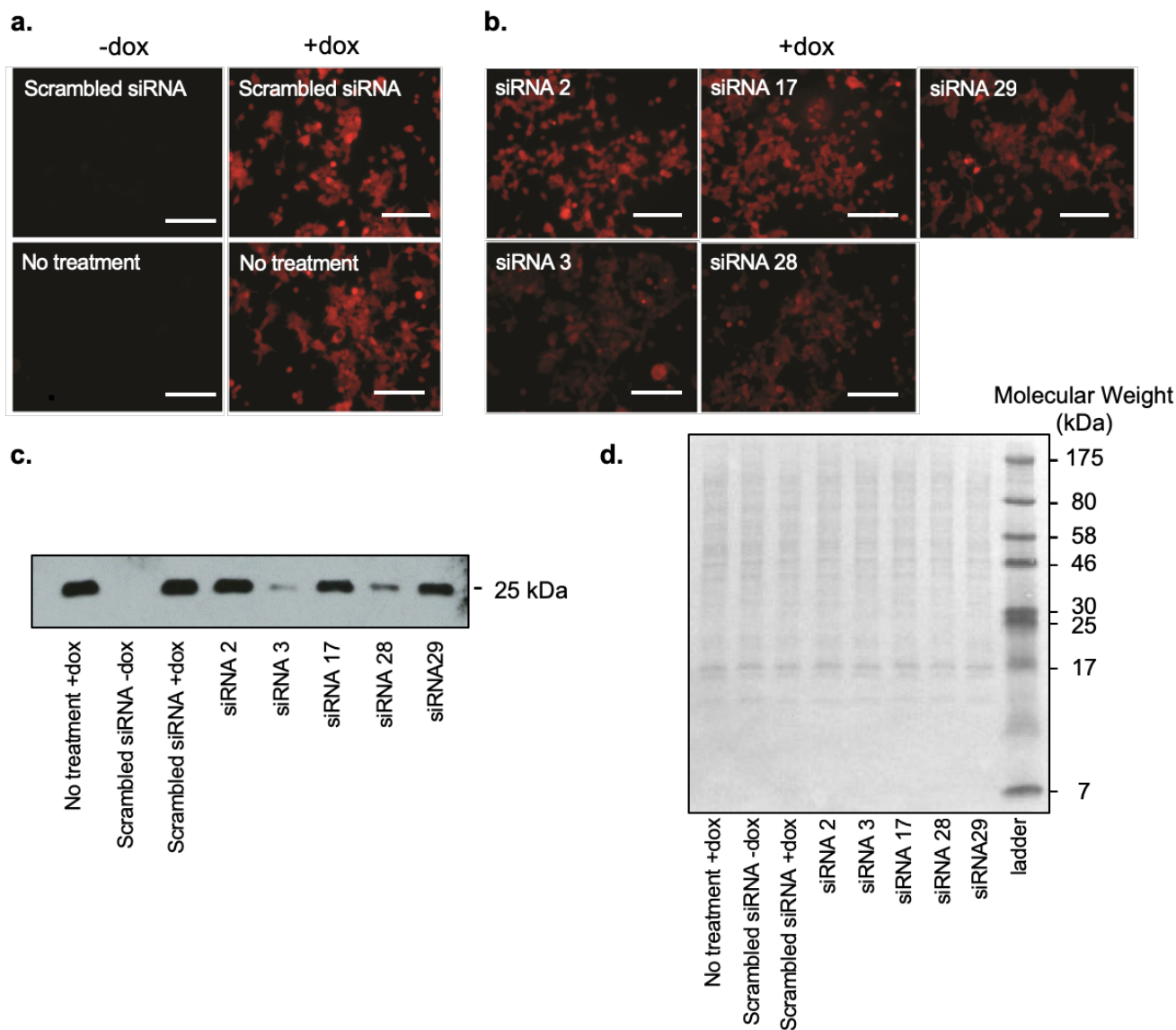
Figure 1 | siRNA design and testing on doxycycline-induced HEK 293-mC cells. a, Optical Microscopy of HEK 293 T-Rex Flp-In-mCherry cells when induced with doxycycline (+dox) and when not induced with doxycycline (-dox) for cells under treatment with scrambled siRNA (top) or without any siRNA (bottom) and lipofectamine. b, Corresponding images of doxycycline induced cells (+dox) transfected with five different siRNA sequences coding for the mCherry gene. c, western blot using anti-RFP antibody for the same conditions as depicted in (a) and (b). Bands represent relative levels of mCherry protein within cells post transfection. d, Ponceau stain evaluating equal effectiveness of loading.

Loading of siRNAs into MOF and characterization

In order to select an optimal Zr-MOF, we performed molecular simulations to find a structure with a porosity compatible with this specific macromolecule; this also allows us to gain insights into how the presence of one double-stranded siRNA 3 molecule affects the energetics of the encapsulating MOF

6

136 system. We considered NU-1000 (Zr_6-based MOF composed of $Zr_6(\mu 3\text{-}OH)_4(\mu_3\text{-}O)_4(OH)_4(OH_2)_4$ nodes

137 and pyrene-based linkers [TBAPy^{4-}, 1,3,6,8-tetrakis(p-benzoate)pyrene];[43] NU: Northwestern

138 University) based on previous experience and the possibility of tuning the particle size into the nm range

139 (which we term nNU-1000). We have previously performed cell toxicity assessments and degradation

140 studies in phosphate buffered saline (PBS) for this particular MOF that verify its biocompatibility and

141 use for these biological applications.[31] We have also verified by proton NMR that the DMF used during

142 the solvothermal synthesis of the MOF, which could negatively impact future biological applications, is

143 completely removed during the purification and activation of the MOF (Figure S2, Supplementary

144 Information). Additionally, the porosity of nNU-1000 is sufficiently large to allow the encapsulation of

145 siRNA 3 within its 3 nm diameter and hexagonal mesoporous channels. **Figure 2a** shows an energy

146 minimized final configuration of an siRNA molecule in nNU-1000 pore model, with a favorable binding

147 energy of -878 kJ/mol; the energies of nNU-1000 with siRNA compared with the isolated systems are

148 located in **Table S2, in the Supplementary Information**. It indicates that there is sufficient free volume

149 for the siRNA and NU-1000 components to pack without distortions as is verified with the favorable

150 (negative) energy, suggesting a thermodynamic preference for the siRNA molecule to be located inside
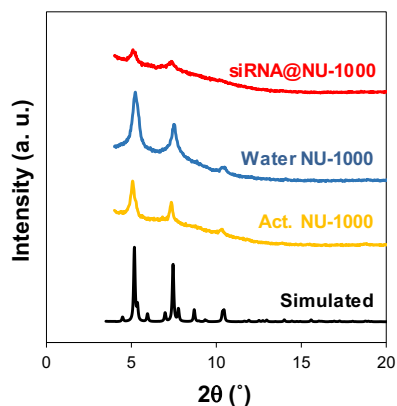
151 the NU-1000 pore channel.

152 We then loaded siRNAs into the MOF nanoparticles – nNU-1000. **Figure 2b** shows the powder X-

153 ray diffraction (PXRD) patterns of nNU-1000 and loaded samples and the comparison with the simulated

154 pattern. The nNU-1000 was activated at 100°C for 3 days to ensure that all potential solvent inside the

155 pore structure was removed. The main peaks are preserved but some minor ones are lost when compared

156 with the calculated pattern; this is compatible with the small particle size of nNU-1000. We then soaked

157 nNU-1000 in RNase free water at the same MOF concentration as our siRNA-loaded sample (20 mg/mL)

158 and observed excellent agreement with the PXRD pattern of the activated nNU-1000. However, the

159 loading of siRNAs in nNU-1000 (siRNA@nNU-1000) led to a decrease in the intensity of the major

peaks. This is consistent with a notion that the siRNAs are adsorbed inside the porous MOF cavity, causing a decrease in the contrast between phases (i.e. the framework and the empty or filled porosity) and therefore a decrease of the peak intensity. The amount of siRNA loaded, measured from the liquid supernatant, was approximately 150 pmol/mg of nNU-1000, as quantified by an RNA-specific fluorescence marker.
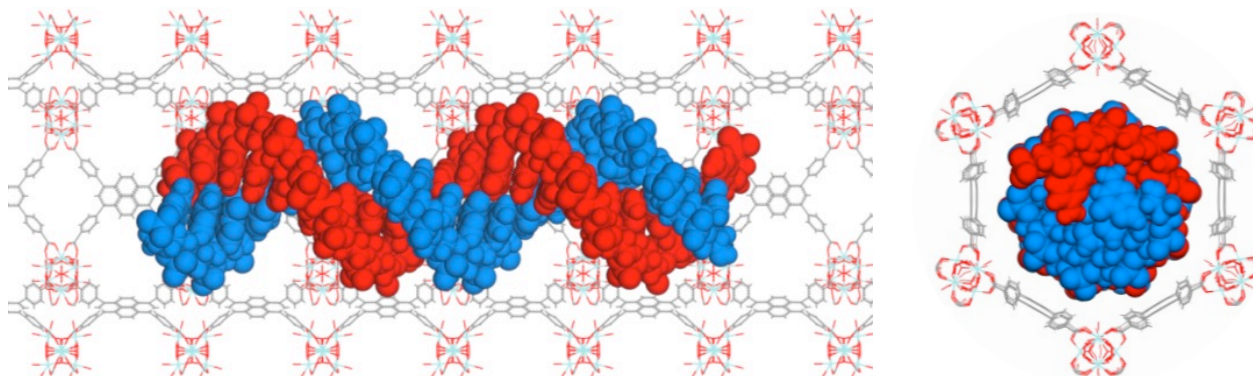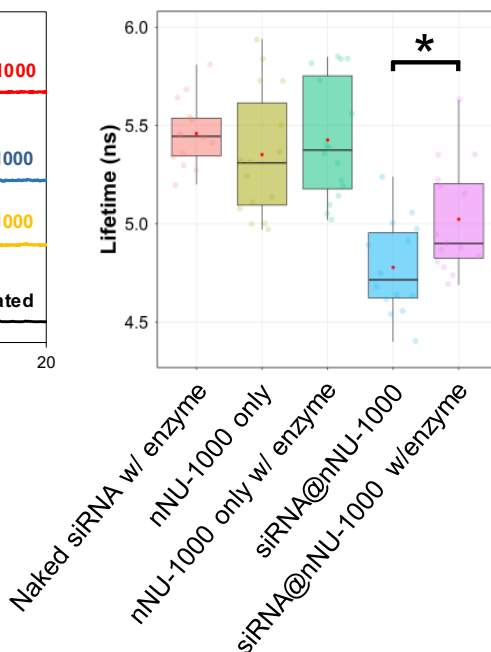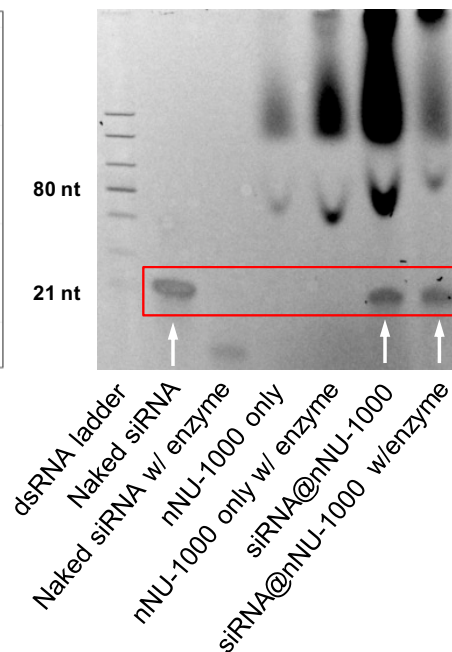

Figure 2 | Encapsulation of siRNAs with NU-1000. a. schematic lateral and top-view of a section of the NU-1000 pore channel with one double-stranded siRNA molecule (red and blue intertwined space filling structure). b. powder X-ray diffraction (PXRD) patterns of simulated NU-1000, activated nNU-1000, nNU-1000 soaked in water and siRNA loaded nNU-1000. c. fluorescence-lifetime imaging microscopy (FLIM) analysis of different systems. Data are shown in box-and-whiskers style, where "box" represents 1st quartile, median, and 3rd quartile, and "whiskers" (lines) represent minimum and maximum values. Averages are represented by the red dots. Individual data points are shown in faint colored circles with outliers as grey circles. 15 lifetime images were

8

acquired per condition. Statistical analysis was carried out using one-way ANOVA followed by Sidak's Multiple Comparisons test (* P<0.05). **d.** 20% TBE polyacrylamide gel stained with PAGE GelGreen for the enzyme degradation protection analysis of different systems. A dsRNA ladder on far right of gel gives location of 21 nucleotide length fragments. White arrows indicate the presence of non-degraded siRNAs.

As mentioned above, enzymatic degradation is one of the major drawbacks in siRNA therapy. The question of whether the siRNAs are located inside the MOF's porosity or outside on the external surface – or in both locations – is therefore critical for its efficient transfection. We first evaluated the localization of the siRNA through fluorescence lifetime imaging microscopy (FLIM). The fluorescence lifetime is sensitive to the micro-environment of a fluorescent molecule[44] and can provide an indirect readout on intermolecular interactions on the scale of a few nanometers. We used time correlated single photon counting (TSCPC) to quantify FLIM signals. Loading MOFs with fluorescently labeled siRNAs results in a drop on lifetime of the intrinsic fluorescence emission from the MOF material because of energy transfer from the dye to the MOF scaffold. We loaded nNU-1000 with a high concentration of siRNAs, using both tagged and non-tagged varieties. We then reacted these samples with an enzyme that can cleave siRNA of 21 nucleotides (nts) in length. Since the enzyme is too large to enter into the porous MOF structure, it will be able to degrade only the siRNAs that are exposed on the external surface of the MOF. **Figure 2c** shows the fluorescence lifetimes for five experimental conditions: nNU-1000 only; siRNA-, untagged or tagged, loaded nNU-1000; and enzyme-reacted siRNA-, untagged or tagged, loaded nNU-1000. The fluorescence lifetime for the MOF alone is 5497 ± 60 ps. This value decreases slightly but not significantly to 5352 ± 80 ps for the untagged-siRNA@nNU-1000, indicating that without the fluorophore, there is no energy transfer and therefore no effect on the MOF's fluorescence lifetime. The enzyme reacted with the untagged-siRNA@nNU-1000 also shows a negligible change in lifetime (5492 ± 80 ps). However, the lifetime of the tagged-siRNA@nNU-1000 drops significantly (P<0.0001) to 4718 ± 80 ps, indicating that the MOF fluorescence is quenched due to a FRET- (Foerster Resonance Energy Transfer) like process between the labeled siRNA and the MOF scaffold it occupies. In the case of the enzyme-reacted tagged-siRNA@nNU-1000, we observed a statistically significant increase (P<0.05) up

199 to 5023 ± 70 ps. This noticeable increase in lifetime from the non-enzyme reacted to enzyme-reacted

200 structure of *ca.* 300 ps suggests that some level of siRNA degradation is occurring. In order for the

201 enzyme to degrade the siRNA, some siRNAs must be located externally on the MOF's surface. However,

202 the more prominent decrease in lifetime of *ca.* 500 ps between the nNU-1000 only and the tagged-

203 siRNA@nNU-1000 with enzyme (P<0.001) suggests that the majority of the siRNAs are loaded in the

204 internal porosity of nNU-1000.

205   To further analyze the capacity of nNU-1000 to protect siRNA, we designed an enzyme protection

206 assay. **Figure 2d** shows the presence of the siRNA, measured on a gel, after exposure to the enzyme

207 described above. As a control, we observed that the 21 nt band in the gel for the naked, unprotected,

208 siRNA disappears when exposed to the enzyme, confirming that this enzyme cleaves siRNA sequences

209 of this length. We also verified that nNU-1000 would not show a false positive band on the gel at the 21

210 nt siRNA location; most of the MOF residue remaining post-purification gets trapped higher up on the

211 gel, with bright and smeared bands at around 80 nt and above, as marked by the ladder. In addition, there

212 is no change in the gel pattern for nNU-1000 reacted with enzyme, demonstrating that the enzyme would

213 not cleave any MOF components to a similar size as the 21 nt band. After purification of the siRNAs

214 from the siRNA@nNU-1000 sample, both with and without exposure to the enzyme, bands are present

215 at the 21 nt location, demonstrating the capability of nNU-1000 to protect the siRNAs from enzymatic

216 degradation.

217 ***In vitro* effect of siRNA on mCherry cell line**

218 With the characterized siRNA@MOF system, we aimed to quantify the signal knockdown and efficacy

219 *in vitro*. We activated the inducible HEK 293-mC cell line with tetracycline and incubated it with various

220 controls along with the siRNA@NU-1000. **Figure 3a** shows the results of the mCherry expression levels

221 normalized to induced HEK 293-mC cells; **Table 1** highlights the first quartile, median, third quartile,

222 and interquartile range (IQR) values for the different experiments. We can first confirm that these cells

do not express mCherry when not induced – in this case expression levels are around 1.2%. This figure also demonstrates the ineffectiveness of the naked siRNAs when added to the cells, as mCherry expression levels did not deviate significantly from those of untreated induced cells. The positive control, siRNA@lipofectamine, shows a significant decrease of 40% in signal compared to the normalized signal from induced HEK 293-mC cells. We also verified that the nNU-1000 did not by itself affect cellular expression levels of mCherry, as the mean value stays near 100%. Interestingly, when we added the siRNA@nNU-1000 complex, we observed a wide range of results. At times, there was no change in the mCherry expression and at other times the mCherry expression would be nearly as low as the positive control siRNA@lipofectamine. In other words, whereas the IQR (i.e. the box height) values for the previous cases was rather low, in the range of 5.7 and 9.4, it significantly increased for siRNA@NU-1000 up to 26.5 (i.e. 219% increment compared to siRNA@lipofectamine). To understand this increase in the variability of mCherry expression levels, we utilized an siRNA tagged with a fluorophore at 647 nm to assess the internalization of the siRNA@nNU-1000 complex in the HEK 293-mC cells. **Figure 3b** shows the fluorescence of Alexa Fluor 647, representing the quantity of siRNAs, normalized to the positive control. As expected, we found minimal fluorescence in normal non-induced cells and induced cells, both without the addition of siRNAs. The observed signal is attributed to auto-fluorescence with no statistical difference between normal non-induced cells, induced cells, cells with naked siRNA added or cells with nNU-1000 only added. This confirms that no siRNA is present inside any of the cells. siRNA@nNU-1000 was taken up into cells nearly as efficiently as siRNA@lipofectamine, but was not as effective at knocking down mCherry expression. Since siRNA must be in the cytoplasm to be effective in its signal knockdown pathway, we hypothesized that the inconsistent and variable levels of mCherry gene knockdown are caused by siRNA@NU-1000 complex entrapment and degradation in endosomes, and that siRNA consequently gets degraded before it is released in the cytoplasm.
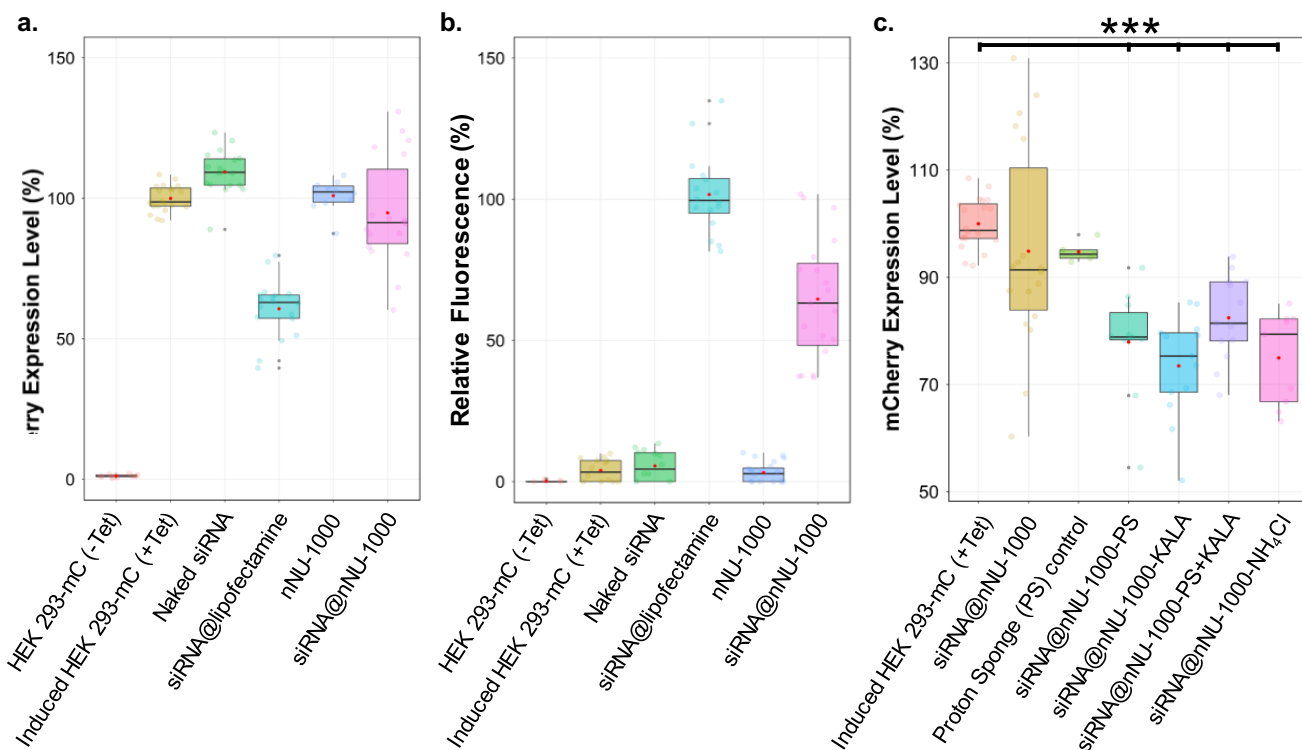
Figure 3 | In vitro performance of siRNAs loaded in NU-1000. **a.** mCherry expression level in HEK 293-mC cells as quantified by flow cytometry after 24 h incubation, **b.** Alexa Fluor 647 fluorescence of siRNA tagged, as quantified by flow cytometry and normalized to positive control, siRNA@lipofectamine and **c.** comparison of mCherry expression level in HEK 293-mC cells when using different co-factors. Plots are shown in box-and-whiskers style, where "box" represents 1st quartile, median, and 3rd quartile, and "whiskers" (lines) represent minimum and maximum values; averages are represented by the red dots. Individual data points are shown in faint colored circles with outliers as grey circles. Each condition was run with a minimum of 9 replicates with some conditions having up to 24 replicates. Statistical significance was calculated through one-way analysis of variance (one-way ANOVA) and a post Dunnett's Multiple Comparison Test compared to the induced HEK-293-mC (+Tet) (*** $P<0.001$).

12

mCherry Expression Levels	Non-induced	Tetracycline-induced	naked siRNA	siRNA@lipofectamine	nNU-1000	siRNA@nNU-1000	Proton Sponge (PS)	siRNA@nNU-1000 -PS	siRNA@nNU-1000 -KALA	siRNA@nNU-1000 -PS+KALA	siRNA@nNU-1000 -NH$_4$Cl
Q1	1	97.2	104.7	57.3	98.7	83.9	93.6	78.3	68.6	78.1	66.8
Median	1.1	98.7	109.3	63	102.3	91.4	94.3	78.9	75.3	81.4	79.4
Q3	1.6	103.7	114.1	65.6	104.4	110.4	95.1	83.4	79.7	89.1	82.2
IQR	0.6	6.5	9.4	8.3	5.7	26.5	1.6	5.1	11.1	11	15.4

268

269   To test the hypothesis of siRNA@NU-1000 entrapment in endosomes, we added to the siRNA@nNU-1000

270 complex various factors including proton sponges or membrane opening peptides that are able to either break or

271 open endosomes.[24,45,46] We used Proton-Sponge® (PS), the amphipathic KALA peptide, and ammonium chloride

272 (NH$_4$Cl). First, we used FLIM on an Oregon Green 488-conjugated dextran – with the size that can enter through

273 clathrin-mediated endocytosis, comparable to the pathway of entry that our nNU-1000 MOF uses – to quantify the

274 capability of these endosomal release factors to avoid endosomal entrapment. Fluorescence lifetime increased

275 significantly with pH (**Figure S3**), These results suggest that the cofactors PS and NH$_4$Cl are acting in a mechanism

276 that is increasing the vesicular pH from its normal value, whereas KALA, on the contrary, a cell-penetrating

277 peptide is not explicitly acting as a proton absorber. **Figure 3c** shows the results of the mCherry expression levels

278 for these complexed systems compared to the untreated induced HEK 293-mC cells. We loaded approximately

279 0.04 mg of the Proton Sponge® cofactor (~2.7 wt.% of the complex), 0.4 µg of the KALA cell penetrating peptide,

280 and 0.1 µmol (or 5.3 µg) of ammonium chloride. We believe that the small cofactors can be on both the external

281 surface and in the internal porosity, whereas KALA is on the external surface due to its large size. The use and

282 incorporation of a cell-penetrating or targeting peptide and complexation of endosomal release cofactors to our

283 siRNA@MOF system is an element of novelty for this study. When the PS was added (siRNA@nNU-1000-PS),

284 the average expression decreased to *ca*. 78% of the normal induced HEK 293-mC cells. Compared to the impact

285   on mCherry expression of the Proton-Sponge® or the nNU-1000 alone, with expression values of *ca*. 95 and 100%,

286   respectively, this decrease is statistically significant (P<0.01 and <0.001, respectively). When using KALA

287   (siRNA@nNU-1000-KALA), we observed a decrease in mCherry signal to *ca.* 73%. Interestingly, when we co-

288   loaded the MOF with both of these compounds (siRNA@nNU-1000-PS+KALA), we observed a reduction to *ca.*

289   82%, a value that is not statistically different to those of siRNA@nNU-1000-PS and siRNA@nNU-1000-KALA.

290   While literature suggested different mechanisms of action for these particular two cofactors, it was not known if

291   there would be a more efficient response if both were included together. Our results indicate that there is not a

292   cumulative effect of the two compounds. When we added a different compound, ammonium chloride, to the

293   siRNA@MOF complex (siRNA@nNU-1000-NH$_4$Cl), we observed mCherry expression at *ca.* 75% of the induced

294   HEK 293-mC cell value. Regardless of the specific cofactor, when complexed together with the siRNA@nNU-

295   1000, they assisted in the gene knockdown capabilities of the system. The relatively high mCherry expression

296   levels for all the systems, including lipofectamine positive control, with knockdown levels below 50% could be

297   related to the long half-life of the protein. Importantly, we were able to reach, in some cases, knockdown effects

298   on par with that of the positive control siRNA@lipofectamine.

299

Super-resolution microscopy analysis of *in vitro* trends

300

301   We performed experiments *in vitro* using structured illumination microscopy (SIM) [31,47] to get a visual picture of

302   the uptake and release processes discussed. **Figure 4** shows 3-color images of HEK 293-mC cells where we have

303   labeled the early endosomes with an RFP marker. In addition, we incubated the cells with either naked Alexa Fluor

304   647-tagged siRNA (**Fig. 4a**), Alexa Fluor 647-tagged siRNA@lipofectamine, the same positive control we used

305   in the previous experiment (**Fig. 4b**); siRNA@nNU-1000 (**Fig. 4c**) and siRNA@nNU-1000-KALA (Fig. 4d). In

306   all images, the tagged siRNAs can be visualized in red, the nNU-1000, when present, is colored in green and the

307   early endosomes are shown in blue. We chose to stain the early endosomes as opposed to other cellular organelles

308   in an attempt to visualize the point at which the siRNA@nNU-1000 complex dissociates from the endosome, as it

309   must do this to effectively deliver the siRNA into the cytoplasm. As determined previously,[31] nNU-1000 requires

310   active transport to enter cells. It was thus expected that the systems with MOF would colocalize with the early

311   endosomes, whereas the naked siRNA and the siRNA@lipofectamine would not. In agreement with our

312   observations from flow cytometry, we observe that little, if any, of the tagged siRNA signal is located

313   intracellularly (**Fig. 4a**). When using siRNA@lipofectamine, we observed a large amount of tagged siRNA

314   intracellularly – but not colocalized with the endosome (**Fig. 4b**). The lack of endosome colocalization is portrayed

315   with the distinctive red marks in the cell. In the case of siRNA@nNU-1000, the complex directly overlaps with

316   early endosomes, shown by white color indicative of 3-color overlap (**Fig. 4c**). Two specific instances of 3-color

317   overlap are pointed out by the white arrows, indicating that both the siRNA and nNU-1000 are contained within a

318   vesicle – meaning the siRNA would be unable to act with the RISC complex in the cytosol and gene knockdown

319   would not occur. In the case of siRNA@nNU-1000-KALA, the white arrow highlights a position of 2-color

320   overlap between the siRNA and nNU-1000, shown by the yellow color instead of white (**Fig. 4d**). This

321   demonstrates an example of an siRNA not trapped within an endosome and able to bind with the RISC complex

322   and initiate the RNAi pathway. The lack of white color (i.e. the 3-color overlap) in **Figure 4d** supports our

323   hypothesis about the endosomal release factors helping the siRNA@nNU-1000 to evade endosomal retention, and

324   also is a representative example image of the trends we noted in **Figure 3**.

325
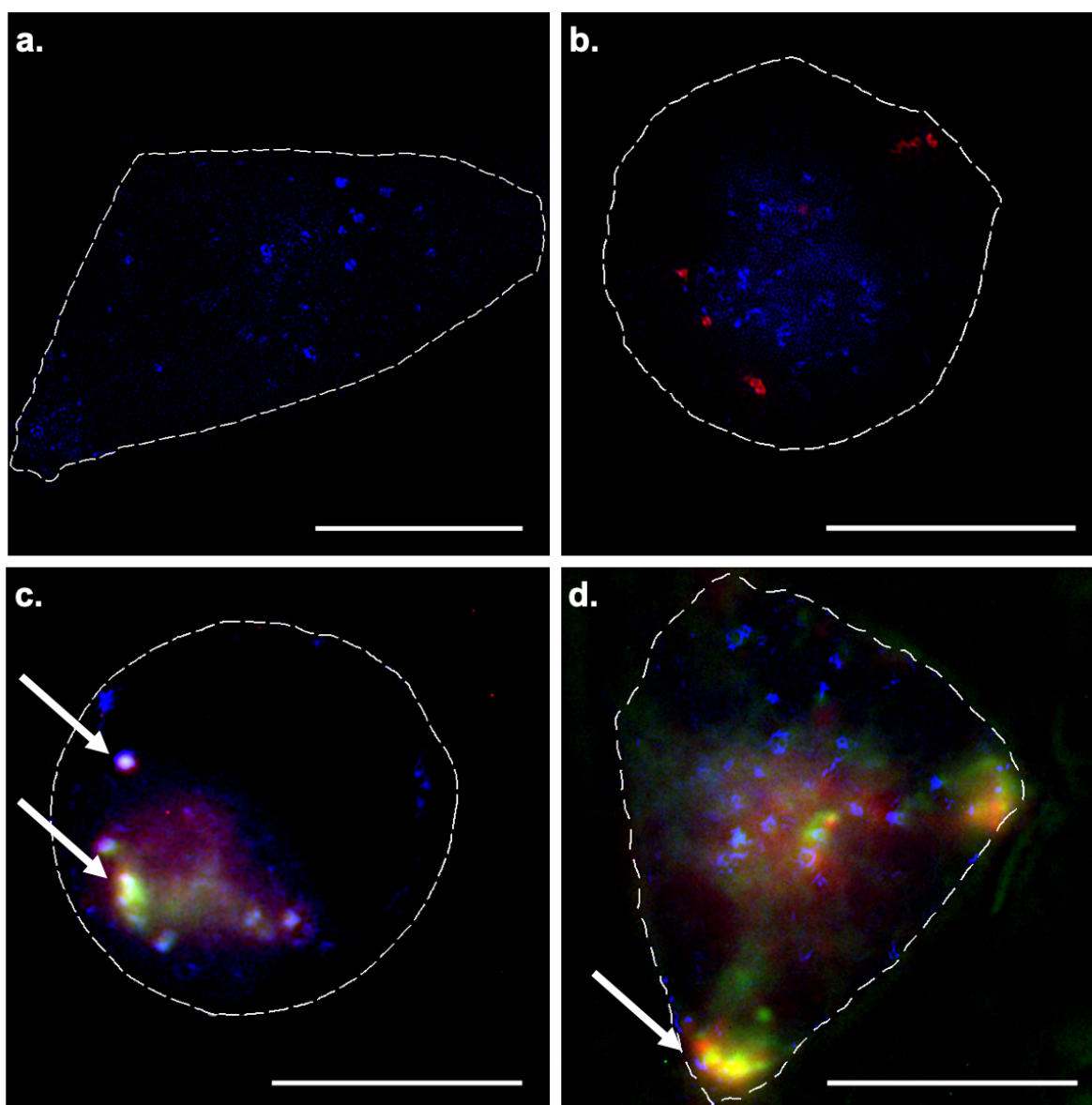
Figure 4 | Representative SIM images of siRNA uptake into HEK 293-mC cells. Images of HEK 293-mC cells incubated with a, naked Alexa Fluor 647-tagged siRNA b, Alexa Fluor 647-tagged siRNA@lipofectamine c, Alexa Fluor 647-tagged siRNA@nNU-1000 and d, Alexa Fluor 647-tagged siRNA@nNU-1000 KALA. Early endosomes stained in blue; Alexa Fluor 647-tagged siRNA in red; nNU-1000 in green. Blue channel taken with SIM; red and green channels taken in wide field. Cell outlines are shown by dashed white lines. Scale bars are 10 µm. The arrows indicate instances of two or three-color overlap.

Conclusions

In this study, we demonstrate the successful development and proof-of-concept efficacy of a Zr-based metal−organic framework, nNU-1000, that is able to load, protect, and deliver siRNA effectively in the cytoplasm to knockdown gene expression. We performed molecular simulations to select the MOF that favored internalization of the siRNA. We characterized the loading of the siRNAs into the MOF by

16

PXRD, where the broadening, decreased intensity, and elimination of some peaks indicated that the siRNAs interacted with the framework in a way that decreased the contrast of the peak intensity, as well as reduced the crystallinity. An enzyme degradation stability study demonstrated that the siRNAs were protected by the MOF, as relevant 21 nt bands were still observed on a polyacrylamide gel after enzymatic attack. We performed studies to elucidate the location of the siRNAs within or on the framework using fluorescence-lifetime imaging microscopy (FLIM). These results suggest that a negligible amount of siRNAs were located external on the MOF's surface, thus the majority of the siRNAs were loaded within the internal porosity of the structure. *In vitro* studies at first suggested that the siRNA was able to enter the cell when carried by nNU-1000, but that efficacy was inconsistent. Based on the hypothesis that this was due to endosomal entrapment, we complexed the siRNA@MOF system with various factors – species that are able to open up endosomes through various mechanisms. By taking advantage of these factors, it was possible to observe consistent levels of knockdown. SIM images show representative examples of the trends we noted in the flow cytometry, and indicate instances along the endosomal uptake pathway at which the siRNA@MOF complex is able to separate from the early endosomes. To the best of our knowledge, this work is the first to utilize a large porous network to internally encapsulate siRNAs in sufficient quantities to achieve gene knockdown –150 pmol/mg MOF. The stability of the MOF material offers future advantages in long-term storage, while the tunability of the MOFs can allow further modifications to improve efficacy. Through this work, we show how the efficacy and efficiency of gene therapy can be improved with implementation of this highly porous material.

Methods

Materials. NU-1000 (also referred to as nNU-1000, 150 nm size) was obtained via synthesis published in previous protocols.[48] Custom siRNA (sense strand 5' – AAGGAGTTCATGCGCTTCAAG – 3') and custom tagged siRNA (sense strand 5' Alexa Fluor 647 tag), was ordered from Eurogentec. HEK 293 T-

rex Flp-In cells were obtained from the ATCC and were modified with a T-REx insert as published in literature.[40] They were cultured with Dulbecco's modified Eagle's medium (DMEM, Sigma-Aldrich D5671), fetal bovine serum (FBS, Sigma-Aldrich F9665), 100× 200 mM L- glutamine (Life Technologies 25030024), penicillin and streptomycin (P-S, Life Technologies 15140122), hygromycin (Thermo Fisher, 10687010, 100 µg/mL final concentration), and blasticidin (Thermo Fisher, R21001, 15 µg/mL final concentration). Phosphate-Buffered Saline (PBS, Sigma D8537) and 1x trypsin−EDTA (Life Technologies 25300054) were used. Trypan blue was purchased from Thermo Fisher (UK, 15250061). Opti-MEM™ Reduced Serum Medium GlutaMAX™ Supplement and Lipofectamine™ RNAiMAX Transfection Reagent were purchased from Thermo Fisher (51985034 and 13778030, respectively). All enzymes and gel ladders used were purchased from New England Biolabs. Novex 20% TBE polyacrylamide gel (EC63155BOX) and Hi-Density TBE Sample Buffer (LC6678, 5X) were bought from Thermo Fisher. A PAGE GelGreen™ Nucleic Acid stain was purchased from Biotium and the Zymo Oligo Clean & Concentrator™ kit was obtained from Cambridge Bioscience (UK, D4061). A Qubit™ microRNA Assay Kit was used (Thermo Fisher Q32880). Stains for endosomes were obtained from ThermoFisher (CellLight Early Endosomes-RFP BacMam 2.0, C10587). Proton-sponge® (99%) was obtained from Sigma Aldrich (158496), and the KALA peptide from AnaSpec (AS-65459). All chemicals and biochemicals used were of analytical grade.

Molecular Mechanics Modeling. A simplified model of the siRNA and nNU-1000 system was constructed in the Materials Studio software package[49] and was created from the NU-1000 crystallographic data published previously.[38] It consists of ten hexagonal rings of Zr-oxide nodes, extended *ca.* 160 Å along the channel. A number of structures were considered, each with different arrangements of the siRNA molecule inside the hexagonal channel of NU-1000. Bonded and non-bonded interactions between all framework atoms were described by the Universal Force Field (UFF),[50] and the structures were optimized using the Forcite module in Materials Studio, using an algorithm that is a

384 cascade of the steepest descent, adjusted basis set Newton-Raphson, and quasi-Newton methods. To

385 estimate the energy associated with the siRNA molecule in NU-1000, we calculated the total energy of

386 the hexagonal channel containing the siRNA molecule ($E_{channel+siRNA}$) and subtracted the energies

387 obtained from the isolated channel ($E_{channel}$) and siRNA molecule (E_{siRNA}) according to: E_{ads} =

388 $E_{channel+siRNA} - E_{channel} - E_{siRNA}$.

389 **X-Ray Diffraction.** Room temperature powder XRD (PXRD) was performed on nNU-1000 loaded and

390 unloaded samples using a Bruker-D8 theta/theta machine with CuKα1 (λ = 1.5405 Å) radiation and a

391 LynxEye position sensitive detector in Bragg Brentano parafocusing geometry. Steps were performed

392 for 2θ = 2˚ to 50˚.

393 **siRNA Adsorption and Subsequent Cofactor Addition.** Samples of nNU-1000 were measured (1.5

394 mg each), and mCherry-encoding siRNA was added in a ratio of 1:2 – tagged siRNA:untagged siRNA –

395 for a total of 15 μL of 10 μM siRNA. The tag was an Alexa Fluor 647 on the 5' end of the sense strand.

396 RNase-free water was added to each such that the final concentration of MOF was 20 mg/mL, and all

397 samples were incubated at 37°C for approximately 2.5 h. Some samples then had a subsequent cofactor

398 addition. For Proton-Sponge®, the calculation was as follows: the amount of metal cluster sites in the

399 MOF sample, in mol, was determined (approximated to one-third the mol of MOF calculated). Half of

400 this molar amount of cluster sites was converted to g of Proton-Sponge® (PS). A solution of PS was then

401 created such that 10 μL of this Proton-Sponge® solution was added to the respective sample. For KALA,

402 10 μL of a 0.04 mg/mL solution in RNAse free water was added to the respective sample. For ammonium

403 chloride, 10 μL of a 10 mM solution in RNAse free water was added to the sample. All samples were

404 incubated for another hour at 37°C. After the 1 h incubation, the samples were centrifuged at 14000 rpm

405 for 60 s, and the supernatant was removed.

406 **siRNA Qubit Quantification.** To quantify the amount of siRNAs in a supernatant solution, we used the

407 Qubit™ microRNA Assay Kit (ThermoFisher Q32880). All samples were purified with the Zymo Oligo

408   Clean & Concentrator™ kit prior to incubation with the Qubit™ Assay kit and measured with the

409   Qubit™ Fluorimeter. 10 µL aliquot of each purified sample was used.

410   **siRNA Enzyme Degradation Stability Analysis.** 5 mg of nNU-1000 were incubated with 75 µL of 10

411   µM untagged siRNA. RNAse free water was added to the mixture such that the final concentration of

412   MOF was 20 mg/mL. Negative controls of naked siRNA and negative controls of MOF only, each with

413   and without enzyme, were also prepared with the same concentration and relative amounts of siRNA and

414   nNU-1000, respectively. The mixture was placed in a 37°C incubator for approximately 2.5 h. The

415   samples containing MOF were centrifuged at 14000 rpm for 60 s, and the supernatant was removed. For

416   those samples that were acting as a negative control for enzyme, 10 µL of NEB Buffer 2 (10x) and 82.5

417   µL of RNAse free water were added to the samples. For the conditions testing enzyme protection, 10 µL

418   of NEB Buffer 2 (10x), 72.5 µL of RNAse free water, and 10 µL of Shortcut RNAse III enzyme were

419   added. All samples were mixed and incubated for 20 min at 37°C before the addition of 10 µL of 10x

420   EDTA. In order to release the siRNAs from the MOF to run on a gel, 100 µL of 10x PBS was added to

421   each sample, and the samples were vortexed until dispersed. Using a Zymo Oligo Clean &

422   Concentrator™ kit, the samples were all purified to remove residue MOF or linker. A Novex 20% TBE

423   polyacrylamide gel was loaded using 8 µL of the purified product of each sample and 2 µL of Hi-Density

424   TBE Sample Buffer (5X). A dsRNA ladder (NEB #N0363S) was also run. The gel was run at 200V for

425   45 min, after which it was soaked in 100 mL of dH$_2$O with 10 uL of PAGE GelGreen™ (Biotium) for

426   approximately 1.5 h. It was imaged using a Syngene G:Box.

427   **siRNA Location Analysis Prep for Fluorescence-lifetime Imaging Microscopy.** Samples of nNU-

428   1000 (*ca.* 0.2 mg) were incubated at 37°C for 2.5 h with either 100 µL of nuclease free water, as a

429   negative control, or 100 µL of 100 µM tagged siRNA. After loading, the samples were centrifuged at

430   14000 rpm for 90 s, the supernatant was removed and used to measure a background, and 200 µL of

431   DMEM without phenol red were added to each of the samples. For the enzyme-reacted sample, 100 µL

432   of the sample loaded with tagged siRNA was spun down again at 14000 rpm for 60 s. The supernatant

433   was removed and 10 μL of Shortcut RNAse III enzyme was added along with 72.5 μL of RNAse free

434   water, and 10 μL of NEB Buffer 2 (10x). This was incubated for 20 min at 37°C before the addition of

435   10 μL of 10x EDTA. This entire sample was then spun down again at 14000 rpm for 60 s, after which

436   the supernatant was removed, and 200 μL of DMEM without phenol red was added to the sample.

437   **Fluorescence-lifetime Imaging Microscopy.** All samples were assayed on a home-built, confocal-based

438   FLIM platform using time-correlated single photon counting (TCSPC). The equipment is a modified

439   version of a published multiparametric imaging system[51] and equipped with a 100x objective lens (UPLS

440   Apo, 100x oil, 1.4NA, Olympus, Germany). A pulsed supercontinuum source (WL-SC-400-15, Fianium

441   Ltd., UK, pulse width 6ps, repetition rate 40MHz) was used for excitation in conjunction with a tuneable

442   filter (AOTFnC-400.650, Quanta Tech, New York, USA), an excitation filter FF01-474/27, and an

443   emission filter FF01-542/27 (both from Semrock Inc., New York, USA). Photons were recorded in time-

444   tagged, time-resolved mode that permits sorting photons from each pixel into a histogram according to

445   the arrival times after the last laser pulse. The laser intensity at the samples was 60 μW. The data were

446   recorded by SPC-830 (Becker and Hickl GmBH, Germany). Photons were acquired for two minutes to

447   make a single 256 X 256 FLIM image. The time-correlated single-photon counting (TCSPC) histograms

448   for each pixel were fitted with a double exponential decay function using FLIMfit[52]. The longer lifetime

449   component τ_2 of the MOF fluorescence decay varied between different conditions and was plotted.

450   Statistical analysis was carried out using one-way ANOVA followed by Dunnett's multiple comparisons

451   test in Graphpad Prism software (La Jolla, California, USA).

452   **Structured Illumination Microscopy (SIM) Imaging.** HEK 293-mC cells were cultured before being

453   seeded at a density of 75,000 cell/mL and 0.4 mL per well on an 8-well LabTek Dish (Thermo Fisher

454   155409) for 1 d. Cells were then incubated with 1.875 μL per well of BacMam Early Endosome Stain

455   overnight. The following day, the entire well contents were removed and the cells were incubated with

the different conditions for MOF prepared following the same protocol described in siRNA Adsorption and Subsequent Cofactor Addition, above. The cells were incubated with these different conditions for 4 h. Post incubation, media was removed from each well, washed once with 1× PBS, and replaced with non-phenol red complete DMEM for SIM Imaging. Images of the samples were collected using a custom built 3-color Structured Illumination Microscopy (SIM) setup which we have previously described.[53] A60×/1.2NA water immersion lens (UPLSAPO 60XW, Olympus) focused the structured illumination pattern onto the sample. This lens also captured the samples' fluorescence emission light before imaging onto an sCMOS camera (C11440, Hamamatsu). Laser excitation wavelengths used were 488 nm (iBEAM-SMART-488, Toptica), 561 nm (OBIS 561, Coherent), and 640 nm (MLD 640, Cobolt), to excite the fluorescence emission of MOF, early endosomes, and siRNA-tag, respectively. The laser intensity at the samples was between 10 and 20 W/cm^2. Upon reconstruction, it was found that the intensity of signal of the MOF and siRNA was too low for artefact-free SIM reconstruction, so widefield reconstruction was used in these channels. SIM reconstruction for the endosome channel was performed in fairSIM,[54] to utilise the latest developments in open-source SIM reconstruction.

siRNA Efficacy Analysis. HEK 293 T-REx Flp-In cells with an inducible mCherry protein, referred to as HEK 293-mC cells, were cultured before being seeded at a density of 140,000 cell/mL with 1 mL per well on a 12-well Nunc Dish (ThermoFisher 150628) for approximately 24 h. The cells were activated with Tetracycline (final concentration: 1 μg/mL) and incubated overnight. While the cells were incubating, different conditions for MOF were prepared as described in siRNA Adsorption and Subsequent Cofactor Addition, above. 1 mL of complete DMEM media was added to each sample. The samples were sonicated for *ca.* 1 min. 200 μL of this solution was added to the respective wells. For the non-MOF conditions (Naked siRNA and siRNA@lipofectamine), 1 mL of complete DMEM media was added to each well prior to adding the following. For the Naked siRNA condition, 3 μL of 10 μM siRNA in a 1:2 ratio – tagged siRNA:untagged siRNA – was added to each well. For the siRNA@lipofectamine

condition, 50 μL of Opti-MEM™ Reduced Serum Medium GlutaMAX™ Supplement was mixed with 3 μL lipofectamine in one tube, and 6 μL of 10 μM siRNA in a 1:2 ratio – tagged siRNA:untagged siRNA –in another tube. 50 μL of each solution was then combined and pipetted briefly before being incubated at room temperature for 5 min. After 5 min, 50 μL of this solution was added to each well. All conditions were left to incubate for 24 h. Post-condition incubation, the media was removed from each well, washed once with 1× PBS, once with trypan blue, twice more with 1× PBS, and then incubated for 5 min at 37 °C with trypsin. Fresh complete DMEM without phenol red was added to the wells after trypsin incubation, and the entire contents were transferred to Eppendorf tubes and centrifuged at 1200 rpm for 5 min. The cells were resuspended in 500 μL of complete DMEM without phenol red. Samples were measured immediately on a Cytek DxP8 analyser cytometer. Analysis was completed with FlowJo software (Becton, Dickinson & Company subsidiary) and Graphpad Prism software (La Jolla, California, USA).

Acknowledgements

References

1. Smith, E. (2016). Tackling hard-to-treat cancers – what, how and why? Cancer Res. UK. Available at: http://scienceblog.cancerresearchuk.org/2016/07/20/tackling-hard-to-treat-cancers-what-how-and-why/ [Accessed April 23, 2018].

2. Cancer Research UK Cancer survival for common cancers. Available at: http://www.cancerresearchuk.org/health-professional/cancer-statistics/survival/common-cancers-compared#heading-Zero [Accessed September 14, 2017].

3. National Cancer Institute (2017). Types of Cancer Treatment. Available at: https://www.cancer.gov/about-cancer/treatment/types [Accessed October 6, 2017].

4. Miller, K.D., Siegel, R.L., Lin, C.C., Mariotto, A.B., Kramer, J.L., Rowland, J.H., Stein, K.D., Alteri, R., and Jemal, A. (2016). Cancer treatment and survivorship statistics, 2016. CA. Cancer J. Clin. *66*, 271–289.

5. American Cancer Society. Cancer Facts & Figures 2019. Atlanta: American Cancer Society; 2019.

6. Noone AM, Howlader N, Krapcho M, Miller D, Brest A, Yu M, Ruhl J, Tatalovich Z, Mariotto A, Lewis DR, Chen HS, Feuer EJ, Cronin KA (eds). SEER Cancer Statistics Review, 1975-2015, National Cancer Institute. Bethesda, MD, https://seer.cancer.gov/csr/1975_2015/, based on November 2017 SEER data submission, posted to the SEER web site, April 2018.

7. He, C., Poon, C., Chan, C., Yamada, S.D., and Lin, W. (2016). Nanoscale Coordination Polymers Codeliver Chemotherapeutics and siRNAs to Eradicate Tumors of Cisplatin-Resistant Ovarian Cancer. J. Am. Chem. Soc. *138*, 6010–6019.

8. Deng, Z.J., Morton, S.W., Ben-Akiva, E., Dreaden, E.C., Shopsowitz, K.E., and Hammond, P.T. (2013). Layer-by-Layer Nanoparticles for Systemic Codelivery of an Anticancer Drug and siRNA for Potential Triple-Negative Breast Cancer Treatment. ACS Nano *7*, 9571–9584.

9. Sudo, H., Tsuji, A.B., Sugyo, A., Ogawa, Y., Sagara, M., and Saga, T. (2012). ZDHHC8 knockdown enhances radiosensitivity and suppresses tumor growth in a mesothelioma mouse model. Cancer Sci. *103*, 203–209.

10. Dykxhoorn, D.M., Palliser, D., and Lieberman, J. (2006). The silent treatment: siRNAs as small molecule drugs. Gene Ther. *13*, 541–52.

11. Whitehead, K.A., Langer, R., and Anderson, D.G. (2009). Knocking down barriers: advances in siRNA delivery. Nat. Rev. Drug Discov. *8*, 129–38.

12. Bobbin, M.L., and Rossi, J.J. (2016). RNA Interference (RNAi)-Based Therapeutics: Delivering on the Promise? Annu. Rev. Pharmacol. Toxicol *56*, 103–22.

13. Dominska, M., and Dykxhoorn, D.M. (2010). Breaking down the barriers: siRNA delivery and endosome escape. J. Cell Sci. *123*, 1183–9.

14. Karnofsky, D.A. (1968). Mechanism of Action of Anticancer Drugs at a Cellular Level. CA. Cancer J. Clin. *18*, 232–234.

15. Wu, S.Y., Lopez-Berestein, G., Calin, G.A., and Sood, A.K. (2014). RNAi therapies: drugging the undruggable. Sci. Transl. Med. *6*, 240ps7.

16. Miele, E., Spinelli, G.P., Miele, E., Di Fabrizio, E., Ferretti, E., Tomao, S., and Gulino, A. (2012). Nanoparticle-based delivery of small interfering RNA: challenges for cancer therapy. Int. J. Nanomedicine *7*, 3637–57.

17. Watts, J.K., Deleavey, G.F., and Damha, M.J. (2008). Chemical modification of siRNA plays an essential role in moving siRNA toward the clinic. Chemically modified siRNA: tools and applications. Drug Discov. Today *13*, 842–855.

18. Chiu, Y.-L., and Rana, T.M. (2003). siRNA function in RNAi: a chemical modification analysis. RNA *9*, 1034–48.

19. Czauderna, F., Fechtner, M., Dames, S., Aygün, H., Klippel, A., Pronk, G.J., Giese, K., and Kaufmann, J. (2003). Structural variations and stabilising modifications of synthetic siRNAs in mammalian cells. Nucleic Acids Res. *31*, 2705–16.

20. Amarzguioui, M., Holen, T., Babaie, E., and Prydz, H. (2003). Tolerance for mutations and chemical modifications in a siRNA. Nucleic Acids Res. *31*, 589–95.

21. Collingwood, M.A., Rose, S.D., Huang, L., Hillier, C., Amarzguioui, M., Wiiger, M.T., Soifer, H.S., Rossi, J.J., and Behlke, M.A. (2008). Chemical modification patterns compatible with high potency dicer-substrate small interfering RNAs. Oligonucleotides *18*, 187–200.

22. Cun, D., Jensen, D.K., Maltesen, M.J., Bunker, M., Whiteside, P., Scurr, D., Foged, C., and Nielsen, H.M. (2011). High loading efficiency and sustained release of siRNA encapsulated in PLGA nanoparticles: Quality by design optimization and characterization. Eur. J. Pharm. Biopharm. *77*, 26–35.

23. Bartlett, D.W., Su, H., Hildebrandt, I.J., Weber, W.A., and Davis, M.E. (2007). Impact of tumor-specific targeting on the biodistribution and efficacy of siRNA nanoparticles measured by multimodality in vivo imaging. Proc. Natl. Acad. Sci. U. S. A. *104*, 15549–54.

24. Schroeder, A., Levins, C.G., Cortez, C., Langer, R., and Anderson, D.G. (2010). Lipid-based nanotherapeutics for siRNA delivery. J. Intern. Med. *267*, 9–21.

25. Jang, M., Kim, J.H., Nam, H.Y., Kwon, I.C., and Ahn, H.J. (2015). Design of a platform technology for systemic delivery of siRNA to tumours using rolling circle transcription. Nat. Commun. *6*, 7930.

26. Patil, Y., and Panyam, J. (2009). Polymeric nanoparticles for siRNA delivery and gene silencing. Int. J. Pharm. *367*, 195–203.

27. Horcajada, P., Gref, R., Baati, T., Allan, P.K., Maurin, G., Couvreur, P., Férey, G., Morris, R.E., and Serre, C. (2012). Metal–Organic Frameworks in Biomedicine. Chem. Rev. *112*, 1232–1268.

28. Xiao, B., Wheatley, P.S., Zhao, X., Fletcher, A.J., Fox, S., Rossi, A.G., Megson, I.L., Bordiga, S., Regli, L., Thomas, K.M., *et al.* (2007). High-Capacity Hydrogen and Nitric Oxide Adsorption and Storage in a Metal−Organic Framework. J. Am. Chem. Soc. *129*, 1203–1209.

29. He, C., Lu, K., Liu, D., and Lin, W. (2014). Nanoscale Metal–Organic Frameworks for the Co-Delivery of Cisplatin and Pooled siRNAs to Enhance Therapeutic Efficacy in Drug-Resistant Ovarian Cancer Cells. J. Am. Chem. Soc. *136*, 5181–5184.

30. Horcajada, P., Chalati, T., Serre, C., Gillet, B., Sebrie, C., Baati, T., Eubank, J.F., Heurtaux, D., Clayette, P., Kreuz, C., *et al.* (2010). Porous metal-organic-framework nanoscale carriers as a potential platform for drug delivery and imaging. Nat. Mater. *9*, 172–8.

31. Teplensky, M.H., Fantham, M., Li, P., Wang, T.C., Mehta, J.P., Young, L.J., Moghadam, P.Z., Hupp, J.T., Farha, O.K., Kaminski, C.F., *et al.* (2017). Temperature Treatment of Highly Porous Zirconium-Containing Metal–Organic Frameworks Extends Drug Delivery Release. J. Am. Chem. Soc. *139*, 7522–7532.

32. Alsaiari, S.K., Patil, S., Alyami, M., Alamoudi, K.O., Aleisa, F.A., Merzaban, J.S., Li, M., and Khashab, N.M. (2018). Endosomal Escape and Delivery of CRISPR/Cas9 Genome Editing Machinery Enabled by Nanoscale Zeolitic Imidazolate Framework. J. Am. Chem. Soc. *140*, 143–146.

33. Chen, Q., Xu, M., Zheng, W., Xu, T., Deng, H., and Liu, J. (2017). Se/Ru-Decorated Porous Metal–Organic Framework Nanoparticles for The Delivery of Pooled siRNAs to Reversing Multidrug Resistance in Taxol-Resistant Breast Cancer Cells. ACS Appl. Mater. Interfaces *9*, 6712–6724.

34. Tamames-Tabar, C., Cunha, D., Imbuluzqueta, E., Ragon, F., Serre, C., Blanco-Prieto, M.J., and Horcajada, P. (2014). Cytotoxicity of nanoscaled metal–organic frameworks. J. Mater. Chem. B *2*, 262–271.

35. Abánades Lázaro, I., Haddad, S., Sacca, S., Orellana-Tavra, C., Fairen-Jimenez, D., and Forgan, R.S. (2017). Selective Surface PEGylation of UiO-66 Nanoparticles for Enhanced Stability, Cell Uptake, and pH-Responsive Drug Delivery. Chem *2*, 561–578.

36. Orellana-Tavra, C., Baxter, E.F., Tian, T., Bennett, T.D., Slater, N.K.H., Cheetham, A.K., and Fairen-Jimenez, D. (2015). Amorphous metal–organic frameworks for drug delivery. Chem. Commun. *51*, 13878–13881.

37. Howarth, A.J., Liu, Y., Li, P., Li, Z., Wang, T.C., Hupp, J.T., and Farha, O.K. (2016). Chemical, thermal and mechanical stabilities of metal–organic frameworks. Nat. Rev. Mater. *1*, 15018.

38. Mondloch, J.E., Bury, W., Fairen-Jimenez, D., Kwon, S., DeMarco, E.J., Weston, M.H., Sarjeant, A.A., Nguyen, S.T., Stair, P.C., Snurr, R.Q., *et al.* (2013). Vapor-Phase Metalation by Atomic Layer Deposition in a Metal–Organic Framework. J. Am. Chem. Soc. *135*, 10294–10297.

39. Cavka, J.H., Jakobsen, S., Olsbye, U., Guillou, N., Lamberti, C., Bordiga, S., and Lillerud, K.P. (2008). A New Zirconium Inorganic Building Brick Forming Metal Organic Frameworks with Exceptional Stability. J. Am. Chem. Soc. *130*, 13850–13851.

40. Lu, M., Williamson, N., Mishra, A., Michel, C.H., Kaminski, C.F., Tunnacliffe, A., and Kaminski Schierle, G.S. (2019). Structural progression of amyloid-β Arctic mutant aggregation in cells revealed by multiparametric imaging. J. Biol. Chem. *294*, 1478–1487.

41. Thermo Fisher Scientific siRNA Design Guidelines | Technical Bulletin #506. Available at: https://www.thermofisher.com/uk/en/home/references/ambion-tech-support/rnai-sirna/general-articles/-sirna-design-guidelines.html [Accessed September 29, 2017].

609 42. Sabel, J., and Integrated DNA Technologies RNAi and DsiRNA: Pathway, mechanism, and design. Available
610   at: http://www.idtdna.com/pages/education/decoded/article/rnai [Accessed April 8, 2018].
611 43. Islamoglu, T., Otake, K.-I., Li, P., Buru, C.T., Peters, A.W., Akpinar, I., Garibay, S.J., and Farha, O.K. (2018).
612   Revisiting the structural homogeneity of NU-1000, a Zr-based metal–organic framework. CrystEngComm *20*,
613   5913–5918.
614 44. Suhling, K., Hirvonen, L.M., Levitt, J.A., Chung, P.-H., Tregidgo, C., Le Marois, A., Rusakov, D.A., Zheng,
615   K., Ameer-Beg, S., Poland, S., *et al.* (2015). Fluorescence lifetime imaging (FLIM): Basic concepts and some
616   recent developments. Med. Photonics *27*, 3–40.
617 45. Cervia, L.D., Chang, C.-C., Wang, L., and Yuan, F. (2017). Distinct effects of endosomal escape and inhibition
618   of endosomal trafficking on gene delivery via electrotransfection. PLoS One *12*, e0171699.
619 46. Varkouhi, A.K., Scholte, M., Storm, G., and Haisma, H.J. (2011). Endosomal escape pathways for delivery
620   of biologicals. J. Control. Release *151*, 220–228.
621 47. Ströhl, F., and Kaminski, C.F. (2016). Frontiers in structured illumination microscopy. Optica *3*, 667.
622 48. Li, P., Moon, S.-Y., Guelta, M.A., Lin, L., Gómez-Gualdrón, D.A., Snurr, R.Q., Harvey, S.P., Hupp, J.T., and
623   Farha, O.K. (2016). Nanosizing a Metal–Organic Framework Enzyme Carrier for Accelerating Nerve Agent
624   Hydrolysis. ACS Nano *10*, 9174–9182.
625 49. Accelrys Software Inc. Materials Studio.
626 50. Rappe, A.K., Casewit, C.J., Colwell, K.S., Goddard, W.A., and Skiff, W.M. (1992). UFF, a full periodic table
627   force field for molecular mechanics and molecular dynamics simulations. J. Am. Chem. Soc. *114*, 10024–
628   10035.
629 51. Frank, J.H., Elder, A.D., Swartling, J., Venkitaraman, A.R., Jeyasekharan, A.D., and Kaminski, C.F. (2007).
630   A white light confocal microscope for spectrally resolved multidimensional imaging. J. Microsc. *227*, 203–
631   215.
632 52. Warren, S.C., Margineanu, A., Alibhai, D., Kelly, D.J., Talbot, C., Alexandrov, Y., Munro, I., Katan, M.,
633   Dunsby, C., and French, P.M.W. (2013). Rapid Global Fitting of Large Fluorescence Lifetime Imaging
634   Microscopy Datasets. PLoS One *8*, e70687.
635 53. Young, L.J., Ströhl, F., and Kaminski, C.F. (2016). A Guide to Structured Illumination TIRF Microscopy at
636   High Speed with Multiple Colors. J. Vis. Exp., e53988.
637 54. Müller, M., Mönkemöller, V., Hennig, S., Hübner, W., and Huser, T. (2016). Open-source image
638   reconstruction of super-resolution structured illumination microscopy data in ImageJ. Nat. Commun. *7*, 10980.